Symmetric Double Proton Tunneling in Formic Acid Dimer: A Diabatic Basis Approach[†]

George L. Barnes, Shane M. Squires, and Edwin L. Sibert III*

Department of Chemistry and Theoretical Chemistry Institute, University of Wisconsin–Madison, Madison, Wisconsin 53706

A model of double proton tunneling in formic acid dimer is developed using a reaction surface Hamiltonian. The surface includes the symmetric OH stretch plus the in-plane stretch and bend interdimer vibrations. The surface Hamiltonian is coupled to a bath of five A_{1g} and B_{3g} normal modes obtained at the D_{2h} transition state structure. Eigenstates are calculated using Davidson and block-Davidson iterative methods. Strong mode specific effects are found in the tunneling splittings for the reaction surface, where splittings are enhanced upon excitation of the interdimer bend motion. The results are interpreted within the framework of a diabatic representation of reaction surface modes. The splitting patterns observed for the reaction surface eigenstates are only slightly modified upon coupling to the bath states. Splitting patterns for the bath states are also determined. It is found that predicting these splittings is greatly complicated by subtle mixings with the inter-dimer bend states.

I. Introduction

Proton transfer is an essential step in many molecular processes.[1] Significant research efforts have been directed toward developing simple models of this transfer in order to identify those representations in which the transfer mechanisms are most apparent. In the condensed phase, the pioneering theories of Hynes and collaborators[1–5] provide a clear example of how choosing the correct representation, in this case the adiabatic representation, can lead to deep insights into the role of solvent in the proton-transfer process. Gas-phase studies have also played an important part in elucidating optimal representations for viewing proton transfer. Tropolone,[6,7] malonaldehyde,[8–11] and formic acid dimer[12–19] (FAD) are well studied examples where a wide range of quantum and semiclassical techniques have been developed to clarify the various factors that contribute to proton tunneling.

In this paper, we investigate a model for the dynamics and spectroscopy of FAD, paying special attention to the tunneling splitting patterns that are associated with the double proton transfer in the gas phase. We have chosen this system for three reasons. First, the intramolecular double hydrogen bond and the corresponding transfer of protons are relevant to large classes of chemical and biological systems.[20,21] Second, this system includes low frequency interdimer modes that have a fundamental influence on the double proton-transfer dynamics, and these modes mimic many of the important solvent motions found in the more relevant condensed phase transfer reactions. Finally, our model is sufficiently simple that we can treat the spectroscopy at a relatively high level of theory and thereby quantify the accuracy of our approximations in choosing to work within various representations.

Given the practical limitations of quantum mechanical calculations of systems consisting of many atoms, it is expedient to pick out those nuclear degrees of freedom (DOF) that are central to the reaction event, these being the reaction surface

or, in the case of just one DOF, the reaction path coordinate. One treats these DOF at a high level of theory, while treating more approximately the remaining DOF and the coupling of them to the reaction surface coordinates. Miller et al.[22] developed the original reaction path Hamiltonian using a curvilinear minimum energy path. For hydrogen transfer reactions, however, the curvature of this path is substantial, and this curvature leads to large kinetic couplings. These couplings are reduced in the diabatic version[23] of the reaction path Hamiltonian by replacing the curved path with a straight line path that connects equilibrium geometries. The tradeoff here is that the large kinetic couplings are replaced with somewhat smaller potential couplings. As an alternative one can use the reaction surface Hamiltonian developed by Carrington and Miller.[11] In their work, the reaction surface for the hydrogen transfer in malonaldehyde is described with two OH bond lengths, whereas the remaining DOF are described using internal coordinates. Tew et al.[8] have recently applied a reaction surface approach to malonaldehyde in which they include coupling between the reaction surface and rotational motions. The computationally demanding aspect of constructing a reaction surface, as opposed to the path, is the calculation of the Hessian along the two versus one DOF. The additional computational work is often needed as Lluch and co-workers have demonstrated the importance of the multidimensional nature of proton-transfer reactions using bidimensional models of proton transfer in tropolone[6] and malonaldehyde.[24]

In this work, we develop a reduced dimensional model of tunneling splittings in FAD that includes 8 A_{1g} and B_{3g} normal modes of the D_{2h} transition state structure. Three of these modes are included in our reaction surface, these being the two in-plane dimer modes and the symmetric OH stretch. The latter mode corresponds to the reaction coordinate at the transition state, yet it is one of the highest frequency modes at an equilibrium configuration. As a consequence, there is no clear time scale separation between these three modes. A simple solution to this problem is provided by using a diabatic representation for FAD. Shin and Light effectively demonstrated

---

* To whom correspondence should be addressed.

the advantages of working in a diabatic representation in the context of H + H$_2$ scattering calculations.[25] In our work, two diabatic surfaces are calculated using the inverse of the empirical valence bond potential (EVB).[26,27] Normally the EVB method is used to construct a global potential surface taking as a starting point the two diabatic potential surfaces that describe the individual dynamics about the two equilibrium geometries. In these diabatic electronic surfaces for FAD, the OH stretch is always the highest frequency mode, and hence, a vibrational adiabatic treatment of the OH stretch mode now provides a faithful representation. This representation allows us to understand readily the central trends found for the tunneling splittings of the surface states. An important result we find is that the splitting pattern found for the low-frequency surface modes demonstrates strong mode specificity; nearly degenerate states have very different tunneling splittings. Moreover these trends persist even when coupling is allowed between the surface modes and the other remaining modes of the model.

Semi-classical instanton and WKB-like[9,10,12−15,28] techniques have been applied to a wide range of double proton tunneling processes. Particularly noteworthy is the theory of Mil'nikov and Nakamura[29] that has been applied to FAD[12] to calculate tunneling splittings of the fundamentals in addition to the ground state. Our study confirms an important finding of that work; excitation of the in-plane interdimer bend increases the tunneling splitting by a factor of 10 from that which is observed in the ground state. For higher frequency fundamentals, our fully quantum calculation points to some risks in applying such theories. Resonant mixing between the fundamentals and combination bands of lower frequency modes leads to splittings that depend sensitively on the details of the potential surface. More generally, given that a recent direct comparison of quantum mechanical and semi-classical treatments in malonaldehyde has raised questions about the accuracy of semi-classical methods in multidimensional tunneling problems,[30] it is important to develop quantum mechanical approaches to calibrate instanton models.

Two recent quantum mechanical studies, related to the present investigation, are the reduced dimensional quantum mechanical models of Luckhaus[17] and Matanović et al.[31] These models have 6 and 5 degrees of freedom, respectively. Luckhaus combines internal coordinates and sequential DVR contractions to calculate the ground state splitting. The very recent work of Matanović et al.[31] is similar to ours both in the choice of coordinates and form of the potential expansion with respect to the RS coordinates. The two bath modes included in that work are different as those workers were mainly concerned with accurate predictions of the ground state and the asymmetric CO stretch tunneling splittings. Experimental measurements of these splittings have been made for both (HCOOH)$_2$ and (DCOOH)$_2$ by Havenith et al.[20,21] In the case of (HCOOH)$_2$, the splittings are reported to be 0.015 and 0.010 cm^{-1}, respectively.

II. Coordinates and Potential

In this section, we present our choice of reaction surface (RS) and bath coordinates and discuss the form of the full dimensional potential expansion. We motivate the basis sets and levels of ab initio theory implemented in these calculations and detail the neural network scheme for fitting the potential points to obtain a surface.

A. Coordinate Choice. We take as our initial coordinate choice the normal modes of FAD evaluated at the transition state (TS). The use of normal modes of the TS versus the equilibrium structure is not a new idea. Bowman et al. point
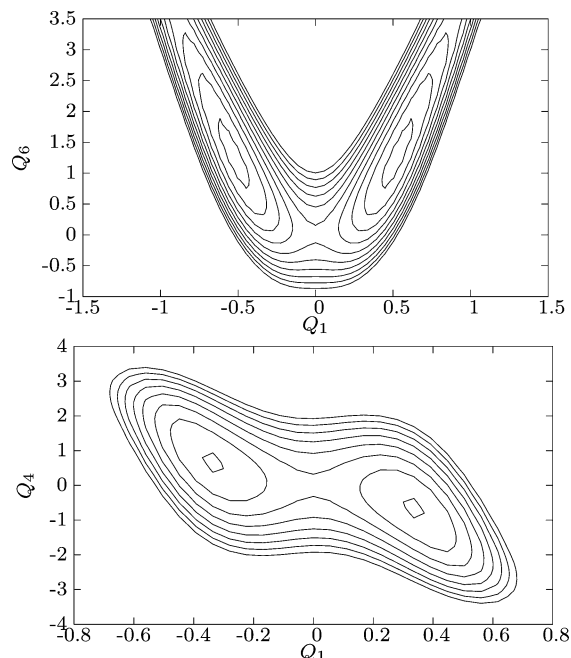

Figure 1. Equipotential contour plots of $V^0(\mathbf{s})$ are displayed as functions of RS coordinates. Contours are separated by 600 cm^{-1}. In each plot, the constant coordinate is fixed to the TS value.

TABLE 1: Transition State Normal Modes

mode	symmetry	character
1	B_{3g}	OH stretch
2	A_{1u}	oop[a] dimer twist
3	B_{3u}	oop butterfly
4	B_{3g}	dimer rock
5	B_{2g}	oop butterfly
6	A_{1g}	dimer stretch
7	B_{2u}	dimer rock
8	A_{1g}	OCO bend
9	B_{1u}	OCO bend
10	B_{3u}	oop CH bend
11	A_{1g}	oop CH bend
12	B_{1u}	OH stretch
13	A_{1g}	oop OH bend
14	B_{3u}	oop OH bend
15	A_{1g}	CO stretch
16	B_{1u}	CO stretch
17	B_{3g}	CH bend
18	B_{2u}	CH bend
19	B_{2u}	OH bend
20	A_{1g}	OH bend
21	B_{2u}	CO stretch
22	B_{3g}	CO stretch
23	B_{1u}	CH stretch
24	A_{1g}	CH stretch

[a] Out-of-plane.

out that the higher symmetry associated with the TS structure simplifies the representation of the potential and the Hamiltonian matrix.[32,33] For similar reasons Seideman et al. use normal modes of the TS pointing out that these coordinates also allow for an easy implementation of the discrete variable representation.[34]

The TS vibrational normal modes are enumerated in Table 1. We find that motion along the reaction path includes large amplitude motion in three of the coordinates, these being the symmetric OH stretch (Q_1), the symmetric dimer rock (Q_4), and the dimer stretch (Q_6). Our RS includes these modes, that we denote using the vector $\mathbf{s} = \{Q_1, Q_4, Q_6\}$.

The role of the RS modes $\mathbf{s}$ can be gleaned from the equipotential contour plots of two-dimensional slices of the

Symmetric Double Proton Tunneling

J. Phys. Chem. B, Vol. 112, No. 2, 2008 **597**

potential shown in Figure 1. The OH stretch coordinate is the reaction coordinate at the TS, and the dimer stretch controls the distance between the proton donor and acceptor. The inclusion of the third coordinate requires more explanation. The double proton transfer in FAD involves the interconversion between the two equivalent minima. During this process, one set of CO double bonds is broken while another set of such bonds is subsequently formed. To accomplish this reaction, the molecule is required to rearrange its heavy atom framework which necessarily involves motion along Q_4. This motion and its coupling to the Q_1, Q_6 surface is characteristic of the reorientation of the solvent during a proton-transfer reaction [cf. Figure 1 of the paper by Staib et al.[1]] We shall see that inclusion of this mode is crucial to our understanding of proton transfer in FAD.

B. Form of the Potential. In our model, the RS modes are coupled to the remaining modes of A_{1g} and B_{3g} symmetry [cf. Table 1]. These modes are referred to as the bath modes. Collectively, we refer to these modes using the vector $\mathbf{b} = \{Q_8, Q_{15}, Q_{17}, Q_{20}, Q_{22}, Q_{24}\}$. When using summations we distinguish RS modes from bath modes by using Greek indices for the former and Roman indices for the latter.

Our strategy, as is the strategy with many RS calculations, is to describe the potential of the RS as completely as possible, treating the bath approximately. We achieve this by expanding the potential in a Taylor series to second order in the bath modes

$$V(\mathbf{s}, \mathbf{b}) = V^0(\mathbf{s}) + W_b(\mathbf{s}, \mathbf{b}) \qquad (1)$$

The zeroth-order contribution is $V^0(\mathbf{s})$, and the first and second-order contributions are combined as

$$W_b(\mathbf{s}, \mathbf{b}) = \frac{1}{2} \sum_{k,k'} [Q_k - Q_{ke}(\mathbf{s})] F_{kk'}(\mathbf{s}) [Q_{k'} - Q_{k'e}(\mathbf{s})] \qquad (2)$$

For each value of $\mathbf{s}$, Hessian elements, $F_{kk'}(\mathbf{s})$, and equilibrium positions, $Q_{ke}(\mathbf{s})$, are calculated using methods described below. As the coordinates included in $\mathbf{s}$ are of either A_{1g} or B_{3g} symmetry, only modes of those symmetry types can have nonzero equilibrium values. For this reason, we expect these modes to be most strongly coupled to the RS.

Tautermann and co-workers[15] have calculated the barrier for proton tunneling in FAD at several levels of theory with a wide range of basis sets. They find that the B3LYP/6-31+G(d) level of theory compares quite well with much higher level CCSD-(T)/aug-cc-pVTZ calculations. Luckhaus[17] further shows that the curvature along his intrinsic reaction coordinate compares favorably with higher levels of theory as well. We make use of Gaussian 98[35] to calculate energies, Hessian elements, and equilibrium positions for a given point, $\mathbf{s}$, at the B3LYP/6-31+G(d) level of theory. The initial step in this process is to determine the equilibrium values of the bath coordinates, $Q_{ke}(\mathbf{s})$. We do this by minimizing the linear forces of the bath DOF.

In fitting the reaction surface Hessian elements and equilibrium positions of eq 1, we make use of a single hidden layer neural network approach which closely follows that of Manzhos et al.[36] A rough grid in $\mathbf{s}$ was first calculated and used to construct a spline fit of $V^0(\mathbf{s})$. From this fit, we selected additional points randomly from an inverse potential distribution for energies below 15000 cm^{-1}. The general functional form of the fits is given as

$$f(\mathbf{x}) = b + \sum_{p=1}^{n} c_p (1 + e^{\mathbf{w}_p \cdot \mathbf{x} + b_p})^{-1} \qquad (3)$$

where n is the number of "neurons", $\mathbf{x}$ are our scaled coordinates, $\mathbf{w}_p$ are weights, and b's are biases. This leads to $5n + 1$ fitting parameters which are solved for using a Levenberg–Marquardt least-squares minimization algorithm. There is no reason that the symmetry present in the fitting data set will be maintained given our choice of coordinates. Therefore, the fit is symmetrized according to

$$\frac{f(\mathbf{x}) + \lambda f(C_{2z}(\mathbf{x}))}{2} \qquad (4)$$

where the C_{2z} operation maps $Q_1 \rightarrow -Q_1$ and $Q_4 \rightarrow -Q_4$ while $\lambda = \pm 1$ depending on the character associated with the C_{2z} operation for the quantity in question. For example, $\lambda = 1$ for the reaction surface while $\lambda = -1$ for $F_{15,22}$. As mentioned above, before fitting all input variables are scaled; the normal coordinates are scaled to lie between $[-1:1]$, and the reaction surface (or Hessian/equilibrium values) is scaled such that all values fall within $[0:1]$ range. The fit coefficients are provided as Supporting Information.[37]

III. Computational Strategy

Herein we describe our calculation of the eigenstates of the RS and the methods implemented to calculate the coupling of the remaining modes to the RS. We start with the $J = 0$ Watson Hamiltonian[38] calculated at the TS. Those vibrational coordinates that are not included in either the RS or the bath are excluded. In addition, we neglect the Watson potential like term and the "vibrational angular momentum" term about the axis perpendicular to the molecule, other components being present only when out-of-plane motion is considered. The latter term, which is more important than the Watson potential term, scales as the rotational constant $C = 0.06$ cm^{-1}, so its neglect is a good approximation. With these approximations our full Hamiltonian is $H = H_s + H_b$ where

$$H_s = \frac{1}{2} \sum_{\alpha} P_{\alpha}^2 + V^0(\mathbf{s}) \qquad (5)$$

and

$$H_b = \frac{1}{2} \sum_k P_k^2 + W_b(\mathbf{s}, \mathbf{b}) \qquad (6)$$

these being the RS Hamiltonian and bath Hamiltonian, respectively.

A. Calculation of RS Eigenstates. We present below a diabatic approach for the calculation of the RS eigenstates. The reason for pursuing such an approach is that the reaction coordinate at the TS corresponds to the high-frequency OH symmetric stretch at the equilibrium configuration. As a consequence, no simple adiabatic separation of the coordinates is possible. One solution to this problem is to follow the approaches utilized in the study of heavy–light–heavy (HLH) systems such as Cl–H–Cl^{-1} where adiabaticity plays a central role and where adiabatic separation can be exploited using hyperspherical coordinates.[39−44] An alternative approach is to work in a diabatic representation. Our approach is similar in spirit to that of Shin and Light[25] and Kubach and Rougeau.[45] The former used this represenation for H + H$_2$ scattering calculation and the latter used it in HLH scattering calculations.

The empirical valence bond potential[26] is a global potential constructed from two potential functions describing small amplitude motion about equilibria. In our study, we proceed in
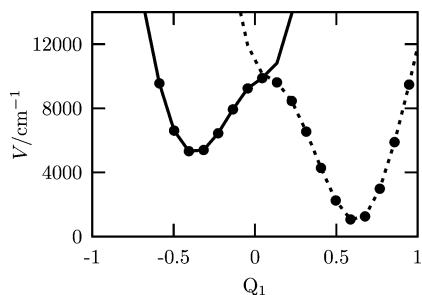
598 *J. Phys. Chem. B, Vol. 112, No. 2, 2008*

Barnes et al.

Figure 2. Plot of the pointwise representation of V^0 (●) as a function of Q_1 with Q_4 and Q_6 fixed at values of -2.04 and 1.15. Also shown are the corresponding diabatic potentials V_L^0 (—) and V_R^0 (---). Surfaces obtained from eqs 7–9 with $(\lambda,\epsilon,\beta) = (50000,200,100)$.

TABLE 2: Grid of Equally Spaced DVR Points Used in RS Calculation

i	N_i	Q_{min}	Q_{max}
1	32	-1.40	1.40
4	28	-3.14	3.14
6	28	-0.58	3.40

the reverse direction, decomposing the RS potential into left and right diabatic contributions as shown in Figure 2. If our surface were a LEPS surface, this separation would have a clear interpretation in terms of coulomb and exchange integrals. Here, however, we follow a pragmatic approach that uses our calculated ab initio surface $V^0(\mathbf{s})$ as the lowest energy solution E_- to the eigenvalue equation

$$\begin{pmatrix} V_L^0 & W \\ W & V_R^0 \end{pmatrix}\begin{pmatrix} \Psi_L \\ \Psi_R \end{pmatrix} = E_\pm \begin{pmatrix} \Psi_L \\ \Psi_R \end{pmatrix} \qquad (7)$$

To calculate the diabatic surfaces V_L^0 and V_R^0, we need to specify the excited-state eigenvalue E_+ and the coupling W. The results are insensitive to the details of the methods, so we describe here just one method employed.

For given values of Q_4 and Q_6, we take slices in Q_1, finding the value of $Q_1 = Q_1^{max}$ for which V^0 takes a maximum value between the two minima. At small values of Q_6 there is no local maximum, and here the minimum value is used. We define the upper adiabatic state energy as

$$E_+ = \lambda(\delta_1^2 + \delta_1^4) + V^0(Q_1^{max}) + \epsilon \qquad (8)$$

and the interaction as

$$W = \beta \exp[-\delta_1^2] \qquad (9)$$

where $\delta_1 = Q_1 - Q_1^{max}$.

Having obtained the diabatic potentials, we solve for the RS eigenvalues using the discrete variable representation (DVR).[46,47] Bačić and Light[46,47] demonstrated the great utility of the DVR, particularly when combined with adiabatic truncation of "fast" coordinates as a function of "slow" coordinates. Using HCN as an example, for each localized bend DVR function (slow) they solved a two-dimensional stretch (fast) Hamiltonian. The corresponding eigenvalues of the fast DOF formed the adiabatic potential surfaces of the bend DOF. The bend basis consists of the eigenfunctions of the corresponding bend Hamiltonian.[46–48] Proceeding in this manner, one builds a compact and efficient basis with which to diagonalize the full Hamiltonian.

We apply a similar approach for the RS of FAD using the potential $V_L^0(Q_1,Q_4,Q_6)$. Here we have two "slow" inter-dimer coordinates (Q_4,Q_6) and one fast (Q_1) coordinate. The primitive

TABLE 3: Select Eigenvalues for the RS Hamiltonian Obtained with the {4,40} Basis[a]

state	ω	Δ	n_1	n_4	n_6
1	0.000	0.006	0	0	0
2	166.232	0.052	0	1	0
3	211.717	0.007	0	0	1
4	333.505	0.218	0	2	0
5	375.326	0.064	0	1	1
6	419.961	0.004	0	0	2
7	502.466	0.569	0	3	0
8	540.364	0.300	0	2	1
9	581.292	0.042	0	1	2
10	625.204	0.002	0	0	3
11	673.209	1.038	0	4	0
12	707.287	0.930	0	3	1
13	744.521	0.192	0	2	2
14	784.501	0.017	0	1	3
15	827.585	0.001	0	0	4
41	2223.484	11.348	1	0	0

[a] Assignments are made via visualization of wave functions.

DVR basis is defined in Table 2. It consists of a set of product sinc functions $|\chi_i^{(1)}\rangle|\chi_j^{(4)}\rangle|\chi_k^{(6)}\rangle$ centered at the points $\{Q_{1i},Q_{4j},Q_{6k}\}$. At each $\{Q_{4j},Q_{6k}\}$ point, we solve for the OH stretch

$$\left[\frac{P_1^2}{2} + V_L^0(Q_1,Q_{4j},Q_{6k})\right]|j_1^{j,k},L\rangle = E_{j_1}^L(Q_{4j},Q_{6k})|j_1^{j,k},L\rangle \qquad (10)$$

retaining the M_1 lowest energy OH stretch eigenvectors $|j_1^{j,k},L\rangle$. Each corresponding eigenvalue $E_{j_1}^L(Q_{4j},Q_{6k})$ forms a potential of a Hamiltonian of slow modes. Denoting the corresponding eigenvectors as $|j_D^{j_1,L}\rangle$, our RS basis is

$$|j_1^{j,k} j_D,L\rangle = |j_1^{j,k},L\rangle|j_D^{j_1}\rangle \qquad (11)$$

the direct product of the lowest M_D eigenvectors of the interdimer Hamiltonian and the corresponding stretch vectors. The D subscript refers to the interdimer modes.

Having constructed the basis for V_L^0, we use the symmetry

$$V_L^0(Q_1,Q_4,Q_6) = V_R^0(-Q_1, -Q_4,Q_6) \qquad (12)$$

to infer the solutions to V_R^0. Plus and minus linear combinations of the left and right vectors are formed to yield the primitive RS bases of A_{1g} and B_{3g} modes, respectively. Using this basis, the eigenfunctions of the RS Hamiltonian are obtained by solving the generalized eigenvalue equation $\mathbf{Hc} = E\mathbf{Sc}$. It is important to note that the left and right functions are nonorthogonal to each other.

B. Inclusion of Bath Modes. Having presented the calculation of the eigenstates of the RS, we now describe how these states couple to the bath DOF. Two methods are considered in this work. In the first, canonical transformations are carried out that lead to simple harmonic basis sets coupled by terms in the kinetic energy operator of the transformed Hamiltonian. In the second, the harmonic basis sets are determined at each of the RS DVR points. Some of the coupling between the bath and the RS modes is found in the nonorthogonality of the basis sets.

1. Method A. There are three canonical transformations we apply in order to reduce the coupling between the RS and bath coordinates. In the first approach, one diagonalizes the force constant matrix $\mathbf{F}$ [*cf.* eq (2)] at each value of the reaction surface using the transformation

Symmetric Double Proton Tunneling

J. Phys. Chem. B, Vol. 112, No. 2, 2008 **599**

$$q_\alpha = Q_\alpha; \quad q_k = \sum_{k'} L_{kk'}(\mathbf{s})[Q_{k'} - Q_{k'e}(\mathbf{s})] \tag{13}$$

This is equivalent to the traditional reaction path approach where one obtains a reaction surface kinetically coupled to normal mode vibrations.

Another approach is to only include the shifts in the equilibrium geometries via the coordinate transformation

$$q_\alpha = Q_\alpha; \quad q_k = [Q_k - Q_{ke}(\mathbf{s})] \tag{14}$$

Here the final Hamiltonian includes kinetic and potential couplings between the harmonic modes. The kinetic energy operator is obtained via the chain rule. As an example, in the transformation of eq 14 the old momenta are written as functions of the new momenta $\{p_\alpha, p_k\}$ as

$$P_k = p_k$$

$$P_\alpha = p_\alpha - \sum_k \frac{\partial Q_{ke}(\mathbf{s})}{\partial s_\alpha} p_k \equiv p_\alpha + \sum_k S_{k\alpha} p_k \tag{15}$$

Here H_b takes the form

$$H_b = \frac{1}{2} \sum_{k,k'} p_k G_{kk'}(\mathbf{s}) p_{k'} + \frac{1}{2} \sum_{k,k'} q_k F_{kk'}(\mathbf{s}) q_{k'} + \sum_k \sum_\alpha [p_\alpha S_{k\alpha} + S_{k\alpha} p_\alpha] p_k \tag{16}$$

where

$$G_{kk'} = \delta_{kk'} + \sum_\alpha S_{k\alpha} S_{k'\alpha} \tag{17}$$

The third transformation shifts the original coordinates by a constant value

$$q_\alpha = Q_\alpha; \quad q_k = [Q_k - \bar{Q}_{ke}] \tag{18}$$

where $\bar{Q}_{ke}$ is the value of $Q_{ke}(\mathbf{s})$ averaged over the ground state wavefunction for the RS Hamiltonian. Since $P_\alpha = p_\alpha$, the simple quadratic form of the kinetic energy operator is unaltered. Defining $q_{ke} = [\bar{Q}_{ke} - Q_{ke}(\mathbf{s})]$, so that $Q_k - Q_{ke}(\mathbf{s})$ equals $q_k + q_{ke}(\mathbf{s})$, the form of the potential $W_b(\mathbf{s,b})$ of eq 2 is simplified to

$$W_b(\mathbf{s,b}) = \frac{1}{2} \sum_k \sum_{k'} \left[F_{kk'}(\mathbf{s}) \right] q_k q_{k'} + \sum_k \left[\sum_{k'} F_{kk'}(\mathbf{s}) q_{k'e}(\mathbf{s}) \right] q_k + \frac{1}{2} \left[\sum_k \sum_{k'} F_{kk'}(\mathbf{s}) q_{ke}(\mathbf{s}) q_{k'e}(\mathbf{s}) \right] \tag{19}$$

where all terms in the square brackets are functions of the RS coordinates. This form has explicit quadratic, linear and constant potential terms with RS dependent expansion coefficients. The linear terms are relatively small, since $q_{ke}(\mathbf{s})$ is small near equilibrium configurations.

In all of these approaches, the bath basis is defined by taking the expectation value of the full Hamiltonian with respect to the ground state RS eigenfunction. The resulting bath Hamiltonian consists of M harmonic oscillators plus additional linear and bilinear coupling terms, depending on which transformation was performed. The bend basis are eigenfunctions of the uncoupled harmonic oscillator Hamiltonian.

2. Method B. Instead of carrying out the transformations of eqs 13−15, one can use three different bath basis functions that are chosen to be eigenfunctions of three different Hamiltonians. Here the Hamiltonians are functions of both bath and RS coordinates.

We now consider the three Hamiltonians in turn. The analogy of eq 13 is for the Hamiltonian to be $H = H_b$. The analogy of eq 14 is for $H = \sum_k H_{bk}$ where

$$H_{bk} = \frac{P_k^2}{2} + \frac{1}{2} F_{kk}(\mathbf{s})[Q_k - Q_{ke}(\mathbf{s})]^2 \tag{20}$$

Finally, the basis set analogy to eq 15 is to modify H_{bk} by removing the bath dependence of the equilibrium configuration such that

$$H_{bk} = \frac{P_k^2}{2} + \frac{1}{2} F_{kk}(\mathbf{s})(Q_k - \bar{Q}_{ke})^2 \tag{21}$$

The bend bases, corresponding to the above three Hamiltonians, successively lead to greater potential coupling, the advantage being that the coupling, due to the nonorthogonality of the bath basis sets evaluated at different $\mathbf{s}$ values, correspondingly decreases.

All matrix elements are calculated using a DVR representation of 41 equally spaced points to describe each one-dimensional harmonic oscillator basis functions. The DVR has the advantage that this representation allows for fast evaluation of overlap integrals. In addition, including anharmonicity in the bath modes would be straightforward with this basis.

In both methods A and B we define the basis by specifying a maximum number of quanta, M_B, to be distributed among the M bath DOF used in that calculation. As such the vector $\{M_B, M_1, M_D\}$ defines our final basis for the full Hamiltonian. If the final matrix size was less than 8000×8000, diagonalization was performed using the Houshoulder method. Otherwise a Davidson method was applied.

In a series of papers, Iung and co-workers[49−52] have demonstrated the utility of the Davidson and block-Davidson methods for calculating highly vibrationally excited states with Jacobi-Wilson coordinates. Our Hamiltonian shares many of the advantages of those coordinates in that it is relatively sparse and easy to evaluate the full Hamiltonian acting on a vector. We attempted to use a hybrid of the block-Davidson scheme, that we developed for finding eigenvalues of Hamiltonians that have been preconditioned with perturbation theory.[53] That method was nowhere near as efficient as the block-Davidson method in the present context.

IV. Results and Discussion

We begin this section by presenting the eigenvalues of the RS Hamiltonian. We emphasize these results, since they provide key insights for understanding the fully coupled model results.

A. Energies and Tunneling Splittings for the RS Hamiltonian. The RS eigenvalues converge quickly in the diabatic basis. The smallest possible basis, i.e., one basis function for each symmetry, yields a ground state (gs) energy of 1417.778 cm^{-1} with a tunneling splitting of about 0.01 cm^{-1}. A $\{4,16\}$ basis (64×64 matrix) yields the converged values of 1416.024 cm^{-1} and about 0.006 cm^{-1}. This corresponds to a decrease of two wavenumbers and a factor of 2 decrease in tunneling splitting when moving from the worst possible basis to a converged result. Clearly this approach is very well suited to the treatment of tunneling problems.

The tunneling splittings of Table 3 show strong mode specific effects. Excitation in the Q_6 DOF has minimal effect in the tunneling splitting, Δ, whereas excitation in the Q_4 DOF
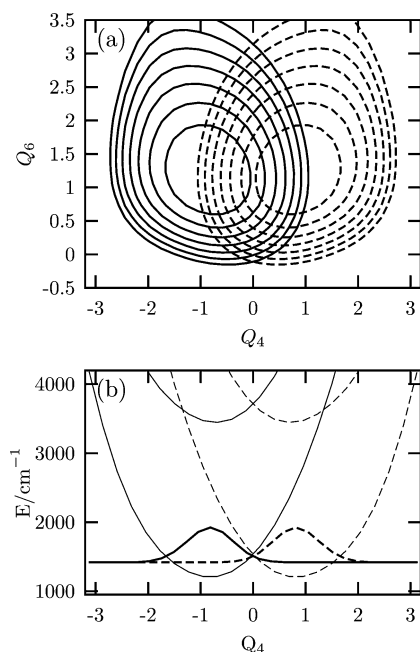
Figure 3. Equipotential curves (a) for the left and right diabatic surfaces corresponding to zero quanta of excitation in Q_1. Curves appear every 500 cm^{-1}. In panel b, slices of these surfaces ($Q_6 = 1.2$) and slices of the ground state wave function for the interdimer DOF are plotted as a function of Q_4. Also shown in (b) are the surfaces corresponding to 1 quantum of excitation in Q_1.

dramatically increases Δ. The ν_4 fundamental has a splitting 10 times greater than the ground state. A noteworthy example of this effect is found in states 10 and 11. These states lie within 50 cm^{-1} of each other, yet the Δ value for the pair of states labeled $|4_4\rangle$ is 520 times larger than that for the $|6_3\rangle$ doublet. Given that Q_6 lies along the reaction coordinate near the equilibrium configuration [cf. Figure 1], this result is at first glance somewhat surprising. One might have expected that excitation in the inter-dimer stretch would be more effective at enhancing tunneling rates due to the decreased O—O distances.[54] This is clearly not the case.

One can understand the trend observed in Table 3 within the framework of the diabatic representation. This representation qualitatively predicts the splitting trend shown in Table 3 for the low lying states even with a basis that does not include excitation in the high frequency Q_1 mode. The key to the explanation is to note that excitation that enhances the overlap between the left and right pair of wave functions will enhance the Δ value. Plotting in Figure 3a the diabatic potential surfaces [cf. eq 10] corresponding to zero quanta of excitation in the OH stretch mode, we observe that excitation in Q_4 clearly leads to enhanced overlap of the left- and right-hand wavefunctions, whereas excitation in Q_6 does not. Figure 3b further illustrates this concept. Slices of both the diabatic surface and the ground state wave function obtained from the surface of Figure 3a are plotted.

We are not the first to note these trends. The factor of 10 enhancement was previously predicted by Mil'nikov et al.[12] using an instanton theory. These workers also note that when they apply the theories of Tautermann and co-workers[15,55] one finds similar results for this low-frequency mode. These theories moreover predict that excitation of ν_6 leads to a slightly diminished tunneling splitting. In contrast to our work, those studies are restricted to excitation of the fundamentals.

The fundamental frequencies of the interdimer bending and stretching modes are calculated to be 166 and 212 cm^{-1},

respectively. Given the level of our ab initio calculations, these numbers are in reasonable agreement with the very recent Raman jet spectroscopy experiments of Zielke and Suhm[56] where these fundamentals are found to be 165 and 194 cm^{-1}, respectively. It should be noted that this study was the first to directly observe the interdimer stretching mode fundamental frequency. In contrast to the OH stretch frequency, which changes dramatically upon inclusion of bath modes, the inter-dimer frequencies are essentially unchanged.

Table 3 reports an OH symmetric stretch frequency of 2223 cm^{-1}. This number contrasts with the experimental number 3035 ± 10 cm^{-1} of Bertie et al.[57] obtained for $(DCOOH)_2$. The poor agreement here should not be viewed as a failure of our force fields; it is a failure of the RS model for treating the symmetric OH stretch. This mode couples significantly to the bath modes via quadratic and Fermi type couplings. Our preliminary calculations with the bath modes included suggest that the intensity of the OH stretch Raman mode will be spread out over many states, and that some of the intensity will be as high as 3100 cm^{-1}. Although an accurate description of this mode is beyond the scope of the current paper, due to its high energy, lower energy states are not. We present below the results of the bath coupling to other DOF.

B. Energies and Splittings of Full Hamiltonian. In section IIIB, we presented two methods for incorporating the bath DOF into the model. In calculations that included select bath degrees of freedom, both the transformation method A and moving basis set method B gave equivalent results. Moreover, neither method offered significant time savings over the other. The great utility of the parallel treatments was in verifying the correctness of the computer codes. In the remainder of the paper we report results obtained with method B.

For each method, three approaches were considered. The first two approaches were less competitive than the third for reasons we now consider. In the first approach [cf. eq 13] one transforms to the bath normal modes at each point of the RS. In contrast to reaction path Hamiltonians where one can readily visualize the avoided crossings that arise as one moves along the reaction coordinate, this is much more difficult in three-dimensions. Furthermore, there are many near resonant bath states, these leading to all the difficulties of seams and conical intersections for nearly degenerate electronic surfaces.[58]

The second approach avoids the above difficulties by defining bath coordinates that simply shift their equilibrium configuration as a function of the reaction surface coordinates [cf. eq 14]. A nice example of an appropriate use of such a coordinate change is found in the work of Staib and Hynes.[59] The leading effect of the transformation is to increase the inverse effective mass of the kth bath normal mode from a value of one by an amount $\sum_\alpha S_{k\alpha}^2$ [cf. eq 11]. When the bath coordinate is high frequency and the RS coordinate low frequency, this transformation approach works well. However, our RS coordinates are not all low frequency, and this in turn leads to a substantial increase in the inverse masses G_{kk}. In the case of mode 8, this increase leads to a normal-mode frequency of about 1000 cm^{-1}. The corresponding converged fundamental frequency of 680 cm^{-1} is only obtained with large bath basis sets.

The final approach, which involves no coordinate change in the bath coordinates beyond a constant shift for the A_{1g} modes, lead to convergence with the smallest bases. It should be noted that mixed approaches were also considered in which some coordinates were transformed as $q_k = Q_k - Q_{ke}(\mathbf{s})$ and others as $q_{k'} = Q_{k'} - \bar{Q}_{k'e}$, but these approaches were no better than

Symmetric Double Proton Tunneling

J. Phys. Chem. B, Vol. 112, No. 2, 2008 **601**

TABLE 4: Mode 8 Results for Various Basis Sets[a]

basis	Δ_{gs}	Δ_8	E_{gs}	ω_8
{4,4,16}	0.0076	0.0086	1838.046	692.502
{4,4,40}	0.0076	0.0068	1838.029	692.491
{4,6,16}	0.0063	0.0080	1837.776	692.472
{4,6,40}	0.0063	0.0063	1837.757	692.460
{5,6,16}	0.0063	0.0081	1837.775	692.415
{5,6,40}	0.0064	0.0064	1837.755	692.403

[a] The basis is defined as $\{M_B, M_1, M_D\}$.

TABLE 5: Full Model Results for RS States

state[a]	ω^b	ω^c	ω^d	Δ^b	Δ^c	Δ^d
1	0.00[e]	0.00	0.00	0.006	0.007	0.007
2	167.28	166.35	166.26	0.058	0.062	0.063
3	209.45	207.42	207.17	0.007	0.007	0.007
4	339.29	334.64	333.93	0.286	0.270	0.273
5	379.67	372.71	371.62	0.118	0.074	0.070
6	423.37	413.66	412.06	0.006	0.004	0.004
7	528.32	508.48	504.50	0.606	0.781	0.740
8	584.78	542.89	538.46	0.527	0.466	0.351
9	619.04	581.36	575.54	0.098	0.070	0.048

[a] See Table 3 for pure RS state notation. [b] Results for basis A with {4,6,16}. [c] Results for basis B with {4,6,25}. [d] Results for basis C with {4,6,40}. [e] Zero-point energies for bases A−C are 5005.310, 5005.145, and 5005.130 cm^{-1}, respectively

TABLE 6: Full Model Results for Bath Mode Fundamentals

state	ω^a	ω^b	ω^c	Δ^a	Δ^b	Δ^c
g.s	0.00	0.00	0.00	0.0064	0.0073	0.0071
8	681.20	681.10	681.18	0.0078	0.0127	0.0896
15	1261.66	1261.49	1261.47	0.0009	0.0024	0.0022
17	1458.63	1458.44	1458.41	−0.0019	−0.0021	−0.0018
20	1410.76	1410.62	1410.62	0.0044	0.0007	−0.0012
22	1706.20	1705.68	1705.49	0.1032	0.1301	0.2001

[a] Results for basis A with {4,6,16}. [b] Results for basis B with {4,6,25}. [c] Results for basis C with {4,6,40}.

the one involving only average coordinate changes, so we do not report results for the mixed approaches.

Model results that couple a single bath mode to the RS were carried out to get an approximate idea of the size of basis sets that might be required with this approach. Mode 8 was seen to converge the most slowly, whereas mode 24 was essentially decoupled. Due to this weak coupling, mode 24 is excluded from the bath DOF. Select results are shown for mode 8 in Table 4. One can see that results appear to be stable with respect to the basis sets considered.

The above results are obtained with direct diagonalization. Extending the coupled modes to include the five bath modes leads to an A_{1g} basis set of 37 800 functions for the basis {5,6,-25}. Converged fundamental states for this basis required 147 iterations with the block-Davidson method. The starting block contained the ground state and the bath fundamentals. When an eigenvalue of the block was converged, that state was excluded in subsequent iterations. The final block-Davidson basis consisted of 423 states.

Results for the RS states are given in Table 5. The striking feature of these results is that the splitting patterns are similar to those of the bare RS Hamiltonian given in Table 3. All of the mode specific effects are retained.

With these mode specific effects in mind, we examine in Table 6 the fundamentals of the 5 A_{1g} and B_{3g} bath modes. Variation with respect to the interdimer mode basis set size is now larger than was seen for the 1 and 2 mode calculations that we performed in the course of this work. This is due to the bilinear coupling between the TS normal modes and the more complex indirect coupling pathways that are available.
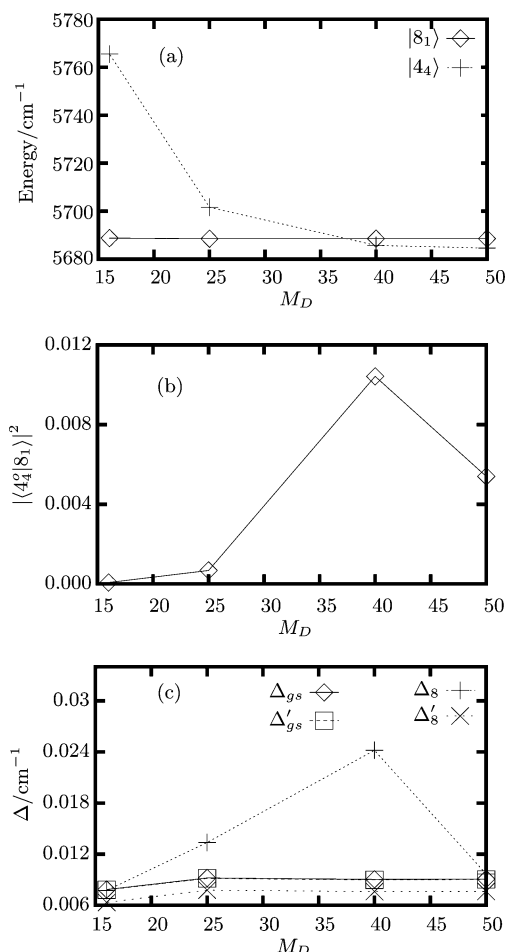

Figure 4. Plots of (a) the eigenvalues for $|8_1\rangle$ and $|4_4\rangle$, (b) the square of the contribution from the primitive $|4_4^o\rangle$ basis function to $|8_1\rangle$, and (c) the splittings for the ground state and $|8_1\rangle$ as functions of M_D. $M_1 = 4$ in all plots. Values with primes denote a calculation where the primitive function $|4_4^o\rangle$ was effectively removed from the basis as described in the text. Removal of the primitive function has little effect on the ground state splitting and clearly shows the source of the surprisingly large splitting seen with $M_D = 40$ in the $|8_1\rangle$ state.

There are several notable trends in the splitting, i.e., modes 15, 17, and 20 have reduced splittings compared to the ground state. Although not shown, this trend holds when M_B is increased from 4 to 5. Here the largest change is in the CO stretch fundamental transition energy that drops from 1410 to 1406 cm^{-1} with a Δ value of 0.002 cm^{-1} for the {4,6,25} basis. Note that these labels are approximate given the important effects of the bilinear couplings.

Some of the Δ fluctuations can be understood, taking the case of mode 8 as an example. In the following, we denote basis states with a superscript o, whereas states without such superscripts are eigenstates with dominate character coming from that particular basis state. As one can see in Table 3 the frequency of $|4_4^o\rangle$ is quite close to the fundamental frequency of mode 8 from the 1 mode calculations. As these two states come into resonance slight mixing will occur. In Figure 4a, the eigenvalues for $|8_1\rangle$ and $|4_4\rangle$ are shown. In this plot, the energy of $|8_1\rangle$ varies by around 0.2 cm^{-1}, which shows that the character of the wavefunction varies only slightly. The energy of $|4_4\rangle$, on the other hand, drops by nearly 80 cm^{-1}. As M_D increases states that previously were not present push $|4_4\rangle$ down in energy. In panel b, we show the square of the contribution of the $|4_4^o\rangle$ basis function to $|8_1\rangle$. As expected the contribution is small for all values of M_D. It is seen that as the energy gap decreases the

contribution increases. Panel c shows the Δ values for two different sets of calculations. We first consider the Δ_{gs} and Δ_8 curves. The ground state splitting shows only small variations, whereas the fundamental splitting increases by a factor of 3 followed by a decrease of nearly the same amount. The behavior of this curve matches that shown in panel b, which strongly suggests that slight mixing with $|4_4^o\rangle$ is the cause. From the bare reaction surface calculations, we know that mode 4 is perfectly suited to promoting tunneling. Those calculations also show that combination states of mode 4 tend to retain the character of the promoting mode. Therefore, it is not surprising that even a very slight increase in the mixing with mode 4 produces dramatically larger tunneling splittings.

To confirm that $|4_4^o\rangle$ is truly the cause of this effect, calculations were performed in which the energy level of $|4_4^o\rangle$ was fixed at a value well above all other states. This effectively removes the state from the calculation and corresponds to the primed curves shown in panel c. The ground state is not affected by the removal of this primitive basis function, while the splitting for $|8_1\rangle$ is now smooth with respect to an increase in the M_D basis. This clearly shows that $|4_4^o\rangle$ is the cause of the erratic behavior that is observed, and these results illustrate the complexity involved with converging the splittings for the fundamentals of the bath modes. One must be concerned not only with building a sufficient basis but also in the location of seemingly benign RS states.

These results highlight an important consequence of the strong mode specificity of the RS states. Given their low frequency, there will often be resonance interactions between RS states and nearby bath state fundamentals. The case of mode 8 was discussed above, but the effect is very general, and it points to the difficulty of predicting tunneling splittings for the bath fundamentals. We caution that potentials that have even small errors in the frequency of the modes may produce erroneous results due to these subtle resonance interactions.

V. Conclusions

We have presented a model for double proton tunneling in FAD. The model consists of a three-dimensional reaction surface Hamiltonian coupled to a bath of the A_{1g} and B_{3g} normal modes excluding the CH stretch. This latter mode was found to be weakly coupled to the former modes. The three modes of the reaction surface are the OH symmetric stretch, Q_1 the reaction coordinate at the transition state, the interdimer stretch Q_6 which controls the distance between the oxygens between which the protons are transferring, and the interdimer, in-plane rocking motion Q_4.

Tunneling splittings are calculated for both the reaction surface Hamiltonian and this Hamiltonian coupled to the bath. The splitting patterns for the low frequency inter-dimer modes, which are similar in both calculations, show strong mode specific effects, where excitation of ν_4 (166 cm^{-1}) enhances the splitting by nearly a factor of 10, whereas excitation of ν_6 (207 cm^{-1}) has little effect. The role of the in-plane rock is readily understood in terms of the diabatic model of the reaction surface vibrations presented within.

This work presents an important step forward in modeling FAD tunneling splittings in that a framework for calculating the splittings is developed, interesting mode specific effects are identified, and the challenges of calculating splitting patterns in the higher frequency bath states are highlighted. Before comparisons can be made with experiment,[20,21] two aspects of the calculation need be addressed. First, it is necessary to incorporate additional modes into the model, the OH asymmetric

stretch being the most important due to its greatly reduced frequency at the transition state compared to the equilibrium configuration. Early work on the inclusion of this mode[19] suggests that one needs to treat it at a higher level of theory than that of a simple harmonic oscillator model, due to the very anharmonic nature of this mode at the transition state. Second, tunneling splittings vary substantially with small changes to the height of the barrier through which tunneling occurs. The barrier in FAD is sensitive to the level of theory and basis set.[14,17,31] For example, in their 5D calculation with a potential obtained at the DFT/B3LYP level of theory, Matanović et al.[31] found that increasing the basis from 6-31+G(d), the basis we used, to 6-311++G(3df,3pd) increases the tunneling splitting of the ground state from 0.0032 to 0.155 cm^{-1}. This increase is primarily due to the barrier heights of 2933 and 2280 cm^{-1} obtained for the respective basis sets.

Supporting Information Available: The fit coefficients. This material is available free of charge via the Internet at http://pubs.acs.org.

References and Notes

(1) Staib, A.; Borgis, D.; Hynes, J. T. *J. Chem. Phys.* **1995**, *102* (6), 2487.

(2) Hynes, J. T.; Tran-Thi, T. H.; Granucci, G. *J. Photochem. Photobiol. A* **2002**, *154* (1), 3.

(3) Kiefer, P. M.; Hynes, J. T. *J. Phys. Chem. A* **2004**, *108* (52), 11793.

(4) Kiefer, P. M.; Hynes, J. T. *J. Phys. Chem. A* **2004**, *108* (52), 11809.

(5) Kiefer, P. M.; Hynes, J. T. *Sol. State Ionics* **2004**, *168* (3−4), 219.

(6) Paz, J. J.; Moreno, M.; Lluch, J. M. *J. Chem. Phys.* **1995**, *103* (1), 353.

(7) Giese, K.; Kühn, O. *J. Chem. Phys.* **2005**, *123*, 054315.

(8) Tew, D. P.; Handy, N. C.; Carter, S. *J. Chem. Phys.* **2006**, *125*, 084313.

(9) Mil'nikov, G. V.; Yagi, K.; Taketsugu, T.; Nakamura, H.; Hirao, K. *J. Chem. Phys.* **2003**, *120* (11), 5036.

(10) Smedarchina, Z.; Siebrand, W.; Zgierski, M. Z. *J. Chem. Phys.* **1995**, *103* (13), 5326.

(11) Carrington, T. J.; Miller, W. H. *J. Chem. Phys.* **1986**, *84* (8), 4364.

(12) Mil'nikov, G. V.; Kühn, O.; Nakamura, H. *J. Chem. Phys.* **2005**, *123*, 074308.

(13) Smedarchina, Z.; Fernández-Ramos, A.; Siebrand, W. *J. Chem. Phys.* **2005**, *122*, 134309.

(14) Smedarchina, Z.; Fernández-Ramos, A.; Siebrand, W. *Chem. Phys. Lett.* **2004**, *395*, 339.

(15) Tautermann, C. S.; Voegele, A. F.; Liedl, K. R. *J. Chem Phys.* **2004**, *120* (2), 631.

(16) Chang, Y. T.; Yamaguchi, Y.; Miller, W. H.; Schaefer, H. F. *J. Am. Chem. Soc.* **1987**, *109* (24), 7245.

(17) Luckhaus, D. *J. Phys. Chem. A* **2006**, *110* (9), 3151.

(18) Shida, N.; Barbara, P. F.; Almlöf, J. *J. Chem. Phys.* **1990**, *94* (5), 3633.

(19) Vener, M. V.; Kühn, O.; Bowman, J. M. *Chem. Phys. Lett.* **2001**, *349*, 562.

(20) Madeja, F.; Havenith, M. *J. Chem. Phys.* **2002**, *117* (15), 7162.

(21) Ortlieb, M.; Havenith, M. *J. Phys. Chem. A* **2007**, *111* (31), 7355.

(22) Miller, W. H.; Handy, N. C.; Adams, J. E. *J. Chem. Phys.* **1980**, *72* (1), 99.

(23) Miller, W. H.; Ruf, B. A.; Chang, Y. T. *J. Chem. Phys.* **89**, 10-(6298).

(24) Bosch, E.; Moreno, M.; Lluch, J. M.; Bertran, J. *J. Chem. Phys.* **1990**, *93*, 5685.

(25) Shin, S.; Light, J. C. *J. Chem. Phys.* **1994**, *101* (4), 2836.

(26) Warshel, A.; Weiss, R. M. *J. Am. Chem. Soc.* **1980**, *102*, 6218.

(27) Chang, Y. T.; Miller, W. H. *J. Phys. Chem.* **1990**, *94*, 5884.

(28) Garg, A. *Am. J. Phys.* **2000**, *68* (5), 430.

(29) Mil'nikov, G. V.; Nakamura, H. *J. Phys. Chem.* **2005**, *122*, 124311.

(30) Coutinho-Neto, M. D.; Viel, A.; Manthe, U. *J. Chem. Phys* **2004**, *121* (19), 9207.

(31) Matanović, I.; Doslić, N.; Kühn, O. *J. Chem. Phys.* **2007**, *127*, 014309.

(32) Bowman, J. M.; Huang, X.; Carter, S. *Spectrochim. Acta Part A* **2002**, *58*, 839.

(33) Huang, X. C.; Carter, S.; Bowman, J. M. *J. Phys. Chem. B* **2002**, *106* (33), 8182.

(34) Seideman, T.; Miller, W. H. *J. Chem. Phys.* **1992**, *97* (4), 2499.

(35) Frisch, M. J.; Trucks, G. W.; Schlegel, H. B.; Scuseria, G. E.; Robb, M. A.; Cheeseman, J. R.; Zakrzewski, V. G.; JMontgomery.; Jr., J. A.; Stratmann, R. E.; Burant, J. C.; Dapprich, S.; Millam, J. M.; Daniels, A. D.; Kudin, K. N.; Strain, M. C.; Farkas, O.; Tomasi, J.; Barone, V.; Cossi, M.; Cammi, R.; Mennucci, B.; Pomelli, C.; Adamo, C.; Clifford, S.; Ochterski, J.; Petersson, G. A.; Ayala, P. Y.; Cui, Q.; Morokuma, K.; Malick, D. K.; Rabuck, A. D.; Raghavachari, K.; Foresman, J. B.; Cioslowski, J.; Ortiz, J. V.; Baboul, A. G.; Stefanov, B. B.; Liu, G.; Liashenko, A.; Piskorz, P.; Komaromi, I.; Gomperts, R.; Martin, R. L.; Fox, D. J.; Keith, T.; Al-Laham, M. A.; Peng, C. Y.; Nanayakkara, A.; Challacombe, M.; Gill, P. M. W.; Johnson, B.; Chen, W.; Wong, M. W.; Andres, J. L.; Gonzalez, C.; Head-Gordon, M.; Replogle, E. S.; Pople, J. A. *Gaussian 98*, revision A.9; Gaussian, Inc.: Pittsburgh, PA, 1998.

(36) Manzhos, S.; Wang, X. W.; Dawes, R.; Carrington, T. J. *J. Phys. Chem. A.* **2006**, *110*, 5295.

(37) See electronic Supporting Information.

(38) Watson, J. K. G. *Mol. Phys.* **1968**, *15*, 479.

(39) Hauke, G.; Manz, J.; Romelt, J. *J. Chem. Phys.* **1980**, *73* (10), 5040.

(40) Kaye, J. A.; Kuppermann, A. *Chem. Phys. Lett.* **1981**, *78* (3), 546.

(41) Babamov, V. K.; Marcus, R. A. *J. Chem. Phys.* **1981**, *74* (3), 1790.

(42) Skodje, R. T. *Annu. Rev. Phys. Chem.* **1993**, *44*, 145.

(43) Nobusada, K.; Tolstikhin, O. I.; Nakamura, H. *J. Chem. Phys.* **1998**, *108* (21), 8922.

(44) Wolf, K.; Mikenda, W.; Nusterer, E.; Schwarz, K.; Ulbricht, C. *Chem. A Eur. J.* **1998**, *4* (8), 1418.

(45) Kubach, C.; Rougeau, N. *J. Mol. Struct. THEOCHEM* **1998**, *424* (1−2), 171.

(46) Bačić, Z.; Light, J. C. *J. Chem. Phys.* **1987**, *87*, 4008.

(47) Bačić, Z.; Light, J. C. *J. Chem. Phys.* **1987**, *86* (6), 3065.

(48) Sibert, E. L.; Mayrhofer, R. C. *J. Chem. Phys.* **1993**, *99*, 937.

(49) Ribeiro, F.; Iung, C.; Leforestier, C. *Chem. Phys. Lett.* **2002**, *362*, 199.

(50) Ribeiro, F.; Iung, C.; Leforestier, C. *J. Theor. Comp. Chem.* **2003**, *2*, 609.

(51) Ribeiro, F.; Iung, C.; Leforestier, C. *J. Chem. Phys.* **2005**, *123* (5), 054106.

(52) Iung, C.; Ribeiro, F.; Sibert, E. L. *J. Phys. Chem. A.* **2006**, *110*, 5420.

(53) Sprague, M. N.; Ramesh, S. G.; Sibert, E. L. *J. Chem. Phys.* **2006**, *124*, 114307.

(54) Loerting, T.; Liedl, K. R. *J. Am. Chem. Soc.* **1998**, *120* (48), 12595.

(55) Tautermann, C. S.; Loferer, M. J.; Voegele, A. F.; Liedl, K. R. *J. Chem. Phys.* **2004**, *120* (24), 11650.

(56) Zielke, P.; Suhm, M. A. *Phys. Chem. Chem. Phys.* **2007**, *9* (32), 4528.

(57) Bertie, J. E.; Michaelian, K. H.; Eysel, H. H.; Hager, D. *J. Chem. Phys.* **1986**, *85* (9), 4779.

(58) Yarkony, D. R. *Acc. Chem. Res.* **1998**, *31* (8), 511.

(59) Staib, A.; Hynes, J. T. *Chem. Phys. Lett.* **1993**, *204* (1−2), 197.